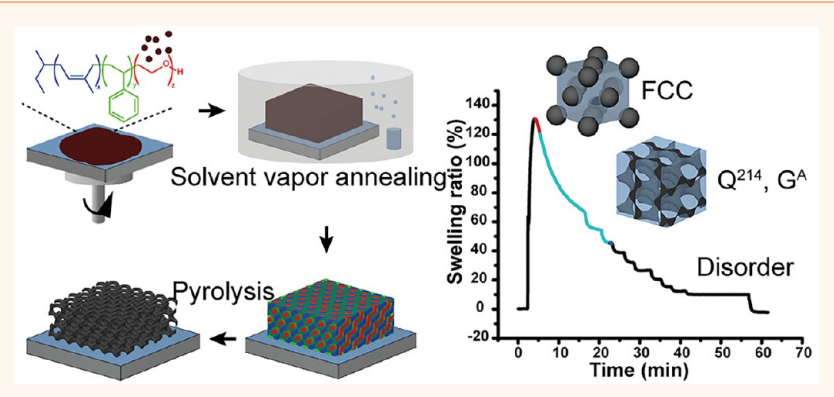


# Pathways to Mesoporous Resin/Carbon Thin Films with Alternating Gyroid Morphology

Qi Zhang,  $^{\dagger}$  Fumiaki Matsuoka,  $^{\dagger}$  Hyo Seon Suh,  $^{\ddagger,\$}$  Peter A. Beaucage,  $^{\dagger}$  Shisheng Xiong,  $^{\ddagger,\$}$  Detlef-M. Smilgies,  $^{\parallel_{6}}$  Kwan Wee Tan,  $^{\dagger,\perp_{6}}$  Jörg G. Werner,  $^{\dagger_{6}}$  Paul F. Nealey,  $^{\ddagger,\$_{6}}$ and Ulrich B. Wiesner\*,†

Supporting Information



ABSTRACT: Three-dimensional (3D) mesoporous thin films with sub-100 nm periodic lattices are of increasing interest as templates for a number of nanotechnology applications, yet are hard to achieve with conventional top-down fabrication methods. Block copolymer self-assembly derived mesoscale structures provide a toolbox for such 3D template formation. In this work, single (alternating) gyroidal and double gyroidal mesoporous thin-film structures are achieved via solvent vapor annealing assisted co-assembly of poly(isoprene-block-styrene-block-ethylene oxide) (PI-b-PS-b-PEO, ISO) and resorcinol/phenol formaldehyde resols. In particular, the alternating gyroid thin-film morphology is highly desirable for potential template backfilling processes as a result of the large pore volume fraction. In situ grazing-incidence small-angle X-ray scattering during solvent annealing is employed as a tool to elucidate and navigate the pathway complexity of the structure formation processes. The resulting network structures are resistant to high temperatures provided an inert atmosphere. The thin films have tunable hydrophilicity from pyrolysis at different temperatures, while pore sizes can be tailored by varying ISO molar mass. A transfer technique between substrates is demonstrated for alternating gyroidal mesoporous thin films, circumventing the need to re-optimize film formation protocols for different substrates. Increased conductivity after pyrolysis at high temperatures demonstrates that these gyroidal mesoporous resin/carbon thin films have potential as functional 3D templates for a number of nanomaterials applications.

KEYWORDS: resols-triblock terpolymer co-assembly, gyroidal mesoporous carbon thin film, 3D templates, film transfer, in situ GISAXS study

aterials with three-dimensional (3D) network structures have demonstrated potential for energy, 1-3 photonics, 4,5 and mechanics 6,7 related applications. The 3D periodic topological features on nano- and micrometer scales endow materials with properties such as negative refractive index<sup>5,8-10</sup> and high strength-to-density ratio.<sup>6</sup> However, direct fabrication of 3D nanostructures made of inorganic materials may be challenging due to limitations in finding suitable direct synthesis methods. Therefore, 3D porous templates are often employed.4

Received: September 10, 2017 Accepted: December 13, 2017 Published: December 13, 2017

<sup>&</sup>lt;sup>†</sup>Department of Materials Science and Engineering, Cornell University, Ithaca, New York 14850, United States

<sup>&</sup>lt;sup>‡</sup>Institute for Molecular Engineering, The University of Chicago, Chicago, Illinois 60637, United States

<sup>§</sup>Materials Science Division, Argonne National Laboratory, 9700 South Cass Avenue, Argonne, Illinois 60439, United States

Cornell High Energy Synchrotron Source (CHESS), Cornell University, Ithaca, New York 14850, United States

<sup>&</sup>lt;sup>1</sup>School of Materials Science and Engineering, Nanyang Technological University, Singapore 639798, Singapore

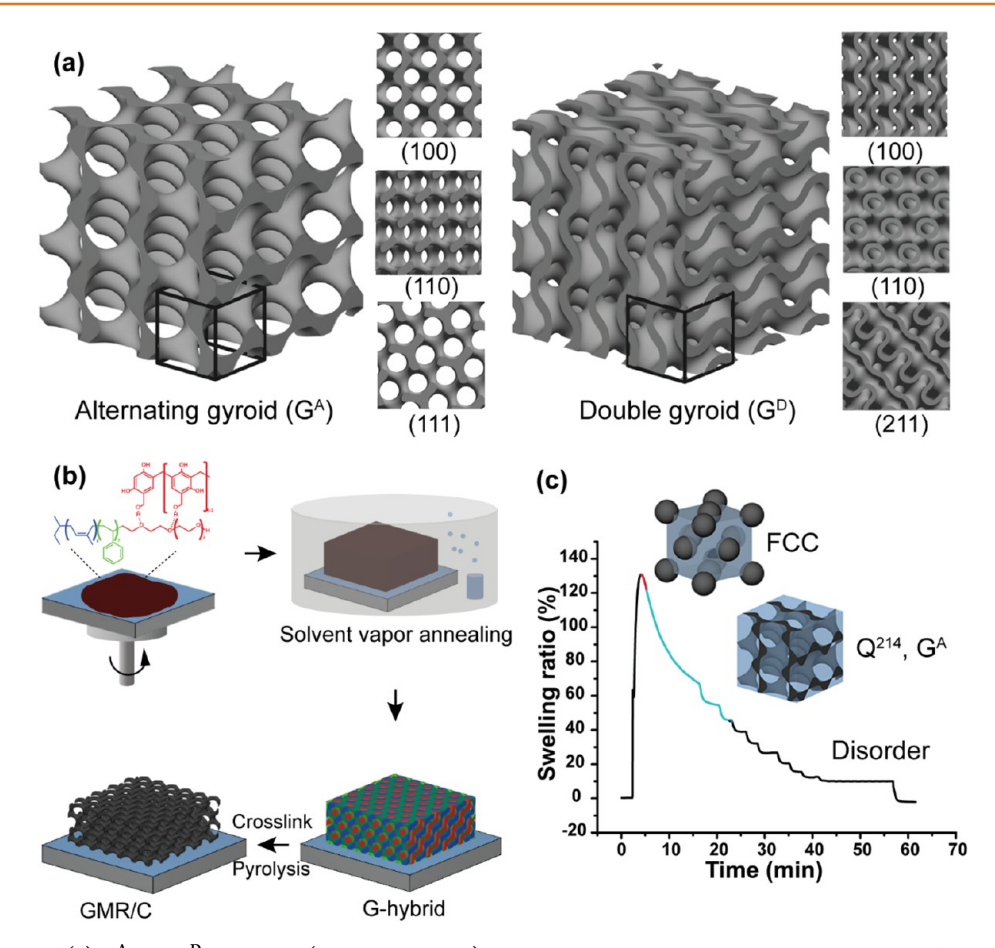


Figure 1. Illustrations of (a) G<sup>A</sup> and G<sup>D</sup> structures (unit cell in black) together with their respective characteristic surface patterns observed for specific crystal planes, (b) GMR/C thin-film fabrication steps, and (c) structure evolution for BCP-resols hybrid thin films during SVA.

Colloidal crystal self-assembly is one of the most popular 3D templating approaches typically generating an inverse opal (IO) structure with face-centered cubic (FCC) symmetry. 11-13 The templates are often made of either polymeric or silica spheres. Various direct laser writing methods are also strong candidates for 3D structure/template fabrication and offer more flexibility in terms of accessible morphologies. 14,15 However, both of these approaches have several drawbacks. First, direct laser writing methods render periodic lattices on length scales typically above 200 nm, while accessing length scales below 100 nm remains very challenging. The second limitation is the lack of versatility in materials choice. The majority of IO structures is derived from polymeric colloids. Similarly, direct laser writing methods as well as 3D printing approaches are often based on photopolymeric materials. Porous polymer templates are suitable for backfilling under mild processing conditions, including atomic layer deposition (ALD) and electrodeposition, but are usually incompatible with approaches requiring high temperatures such as chemical vapor deposition (CVD).<sup>16</sup>

Block copolymer (BCP) self-assembly (SA) enables access to structures below 100 nm. Among the various mesoscale morphologies formed, 3D interconnected networks such as gyroidal structures are of particular interest (see models in Figure 1a). By etching or otherwise removing one of the blocks, the resulting porous polymeric gyroidal templates can subsequently be backfilled with other materials. For example, electroand electroless deposition 22,23 methods have widely been used to deposit metals into these mesoporous polymeric templates. However, incompatibilities exist between these materials and

processes that require high temperatures, strong acids, or organic solvent environments. Such conditions imposed by backfilling processes largely narrow down the choice of materials that can be grown into the templates, thereby limiting their possible applications. In order to overcome these limitations, resorcinol or phenol formaldehyde resols-based carbon networks have been studied in bulk and in thin films.<sup>24–30</sup> To the best of our knowledge, however, mesoporous resin/carbon thin films with periodic single (alternating) gyroidal (Q<sup>214</sup>) structure, which as a result of the large pore volume fraction are particularly interesting as 3D porous templates (e.g., compare structures in Figure 1a), have not been reported to date. This may be due to the complexity of the associated structure formation pathways resulting from such multicomponent systems and factors (e.g., surface energy) predominant in thin films. Pathways may include order-order and/or order-disorder transitions, but have not been elucidated in such composite thin films to date. Moreover, in all of the previous examples, self-assembly of gyroidal structures was optimized for specific substrates. It is wellknown, however, that BCP self-assembly in thin films is strongly influenced by substrate BCP interactions.<sup>31</sup> Results are therefore not transferable from one substrate to another requiring timeconsuming re-optimization of film formation protocols between different substrates. A common approach to overcome such substrate restrictions involves film transfer techniques using a polymeric protective layer.<sup>32–35</sup> To the best of our knowledge, however, such transfer techniques have never been applied to the very open gyroidal porous structures, in particular with alternating gyroid structure.

Table 1. ISO Terpolymer Compositions and Resols Loading Details

polymer	$M_{\rm n}$ (kg/mol)	$f_{\rm PI}$ (vol %)	$f_{\rm PS}$ (vol %)	$f_{\rm PEO}~({ m vol}~\%)$	PDI	PEO + resols (wt %)	resols/ISO <sup>a</sup>	resols type
ISO77-G <sup>A</sup> MR	77	30.6	60.8	8.6	1.04	25	0.26	resorcinol-formaldehyde
ISO69-G <sup>A</sup> MR	69	33.1	62.0	4.9	1.04	25	0.32	resorcinol-formaldehyde
ISO28-G <sup>D</sup> MR	28	10.5	34.1	55.4	1.11	76	0.94	phenol-formaldehyde
<sup>a</sup> Weight ratio.								

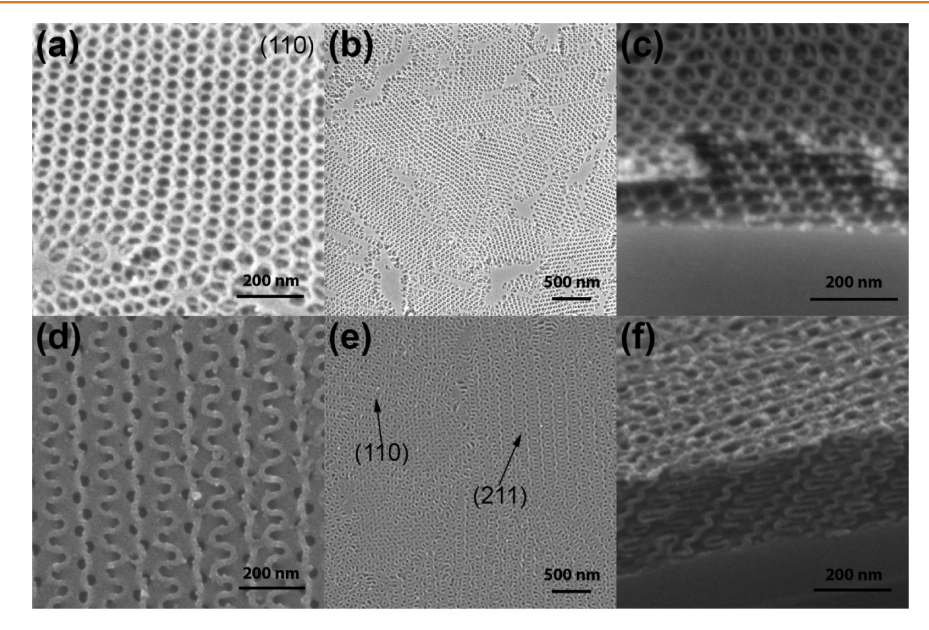


Figure 2. SEM characterization of GMR thin films with (a-c) alternating (ISO77- $G^AMR$ ) and (d-f) double gyroidal (ISO28- $G^DMR$ ) structures. Arrows in (e) indicate grains with specific orientations.

Here we report both single (alternating) gyroid (Q<sup>214</sup>) and double gyroid (Q<sup>230</sup>) mesoporous thin-film 3D structures from solvent vapor annealing (SVA) induced poly(isoprene-blockstyrene-block-ethylene oxide) (PI-b-PS-b-PEO, ISO) triblock terpolymer directed self-assembly of resorcinol/phenol formaldehyde resols as evidenced by scanning electron microscopy (SEM) and grazing-incidence small-angle X-ray scattering (GISAXS). In particular, for resin/carbon thin films with desired large area single/alternating gyroid  $(Q^{214})$  morphology, we show how in situ GISAXS can be employed to elucidate and navigate the pathway complexity of the associated structure formation processes during vapor annealing. With subsequent cross-linking and pyrolysis steps, either 3D gyroidal mesoporous resin-based (GMR; when heated to 450 °C) or carbon-based (GMC; when heated to 600 °C and above) thin films are obtained. Film pore size is tailored by using terpolymers with different molar mass. The pore surface hydrophilicity is tuned by pyrolysis temperature, an ability that may become crucial for backfilling of such intricate 3D structures with different materials. Increasing pyrolysis temperatures also leads to increasingly conducting functional carbon thin films. Finally, we demonstrate that these alternating gyroidal mesoporous thin films can be transferred to arbitrary flat substrates, removing the need for lengthy reoptimization of thin-film structure formation protocols for every new substrate.

# **RESULTS AND DISCUSSION**

**G<sup>A</sup>MR and G<sup>D</sup>MR Thin Films.** Three ISO triblock terpolymers were synthesized to serve as structure directing agents (Table 1). Resorcinol-/phenol-formaldehyde resols served as carbon precursors hydrogen bonded to PEO, thereby

selectively swelling this block. By adjusting block copolymer (BCP) composition and resols loading, two types of network structures with either single/alternating gyroid or double gyroid structure (space groups Q<sup>214</sup> and Q<sup>230</sup>, respectively) were achieved as detailed in Table 1. The composition selections for single and double gyroid structures were based on previous work on bulk ISO-resols composites, which in turn were based on a published ISO morphology map. <sup>24,36</sup> Models of these network structures are shown in Figure 1a for illustration purposes.

The different processing steps of gyroidal mesoporous resin (GMR) thin films with either alternating gyroid (GAMR) or double gyroid (G<sup>D</sup>MR) ordering are illustrated in Figure 1b. In step 1, a solution of ISO BCP and resorcinol/phenolformaldehyde resols was spin-coated onto a Si wafer piece resulting in a thin film with thickness of around 400 nm. In step 2, as-spun films were solvent annealed in THF vapor (Q214) or chloroform vapor (Q<sup>230</sup>) under various conditions (vide infra) until the desired structure was achieved. In step 3, the resulting BCP-resols hybrid thin films were brought to 115 °C to thermally cross-link the resols thereby further locking in the desired film structure. In step 4, a heat treatment at 450 °C under inert atmosphere further condensed the cross-linked resols into the final polymeric resin material while simultaneously decomposing the structure directing ISO terpolymer, resulting in the desired G<sup>A</sup>MR or G<sup>D</sup>MR thin films. In order to help identify films at different processing stages, BCP-resols hybrid thin films during or after SVA, but before the thermal cross-linking step, will be referred to as either BCP-resols hybrid or GA/GD-hybrid, respectively (see Figure 1b), depending on whether the structure has already been converted to a gyroid or not. In the case of the alternating gyroid morphology, structure evolution under SVA

was studied and optimized utilizing a combination of *in situ* reflectometry and *in situ* GISAXS measurements of film thickness and structure, respectively. The resulting data are summarized in graphs, as shown in Figure 1c, where film thickness as a function of time is correlated to film structure. In general, THF vapor pressure was first raised to a high level to ensure a highly swollen film. The film was then deswollen by gradually decreasing solvent vapor pressure over a period of 60 min, while *in situ* GISAXS measurements simultaneously captured structural details as a result of these changes, revealing both order-to-order as well as order-to-disorder transitions as described in detail in the subsequent section.

Scanning electron microscopy (SEM) images of the two types of final GMR thin-film structures (GAMR, GDMR) are shown in Figure 2. Figure 2a-c depicts the ISO77-GAMR thin-film top surface structure at two different magnifications (a,b) as well as a film cross-sectional structure (c). The highly ordered pattern observed in the top surface SEM in (a) clearly resembles the (110) plane of the G<sup>A</sup> model shown in Figure 1a (see Figure S3 for a more detailed analysis). A lower magnification top surface SEM image in Figure 2b reveals the film's grain structure demonstrating its polycrystalline nature. Within each grain, the surface orientation stays along the [110] direction. The crosssectional image in Figure 2c confirms that the mesoporous structure is highly ordered in 3D. More cross-sectional images are shown in Figure S4. Interestingly, these cross-sectional images suggest that the pores are directly accessible at both substrate and air interfaces without the presence of dense capping layers.

Figure 2d–f shows similar SEM images for an ISO28-G<sup>D</sup>MR thin film. The top surface SEM in Figure 2d shows the (211) plane with the characteristic double wavy pattern of the G<sup>D</sup> morphology (compare with model shown in Figure 1a). A lower magnification SEM image in Figure 2e reveals several grains of the polycrystalline film morphology including a grain with (211) surface plane on the right and (110) surface plane on the upper left. The cross-sectional image in Figure 2f demonstrates that the bicontinuous double gyroid structure is maintained throughout the entire film thickness. Films with final G<sup>D</sup> morphology were solvent annealed in a different setup from G<sup>A</sup> films (see Methods section). Their final structure may be a collective result of both SVA and thermal cross-linking, as described in an earlier study.<sup>28</sup>

GISAXS was employed to gain more insight into the structure of G<sup>A</sup>MR thin films and possible deviations from ideal behavior. A 2D GISAXS pattern for a G<sup>A</sup>MR thin-film structure directed by ISO77 is shown in Figure 3. The diffraction pattern was analyzed using GIXSGUI, a Matlab-based tool for visualization, reduction, and indexing of grazing incidence X-ray scattering data.<sup>37</sup> A previous study has shown that the alternating gyroid belongs to the space group #214 ( $Q^{214}$ ) and has  $I4_132$  symmetry.<sup>38</sup> Therefore, the basis coordinates were selected based on space group #214 during indexing. The film normal direction was chosen as [110] based on our SEM results (vide supra, Figures 1a, 2a, and S3). Although space group #214 is cubic, shrinkage along the film normal [110] direction distorts the unit cell and therefore makes the lattice parameters a, b, c,  $\alpha$ ,  $\beta$ ,  $\gamma$  deviate from the cubic lattice rule (a = b = c,  $\alpha = \beta = \gamma = 90^{\circ}$ ). A unit cell of the GA structure is drawn in Figure S5 to better illustrate the influence of shrinkage on the lattice parameters. After shrinkage along the [110] direction, the modified unit cell has a = b < c and  $\alpha = \beta = 90^{\circ}$ , while  $\gamma > 90^{\circ}$ . With these prerequisites and trial and error in indexing GISAXS diffraction patterns, a set of unit cell parameters, a = b = 51.6 nm, c = 71.0 nm,  $\alpha = \beta = 90^{\circ}$ ,  $\gamma = 151.4^{\circ}$ 

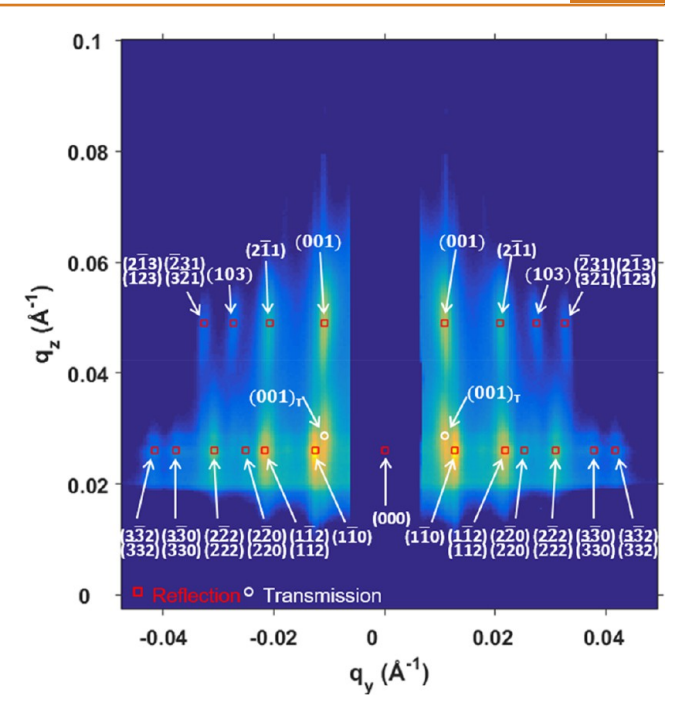


Figure 3. GISAXS pattern and associated indexing for sample ISO77- $G^AMR$ . The incident angle for this data acquisition was  $0.13^{\circ}$ .

rendered a very good match to the measured GISAXS pattern as shown in Figure 3. A shrinkage of 75% along the film normal [110] direction was estimated from this data analysis. Such large shrinkage has been observed before and is expected to be the result of a combination of SVA, thermal cross-linking, and pyrolysis. <sup>18,39</sup> GISAXS experiments were also conducted on an ISO69-G<sup>A</sup>MR film with a GISAXS pattern shown in Figure S6. Using a similar indexing procedure as described above, a shrinkage of 77% was determined for this film. All GISAXS experiments corroborated structure and orientation assignments of G<sup>A</sup>MR thin films by SEM. Since in comparison to the local scale of SEM the GISAXS X-ray beam footprint is on the millimeter scale, these results suggest that G<sup>A</sup>MR nanostructures imaged by SEM were representative for the entire film.

Pathway to Thin Films with G<sup>A</sup> Morphology *via* Structure Evolution during Solvent Vapor Annealing. In comparison to the double gyroid structure (G<sup>D</sup>, Q<sup>230</sup>), which has been observed in both diblock copolymers and triblock terpolymers, the alternating gyroid (G<sup>A</sup>, Q<sup>214</sup>) structure is a network phase unique to triblock terpolymers. From Figures 1 and 2, G<sup>A</sup>MR structures are expected to be more open as compared to G<sup>D</sup>MR structures, which is advantageous as templating scaffolds. Therefore, in this section we will focus on alternating gyroid thin-film formation with particular emphasis on the structural evolution and associated pathway complexity during SVA on the way to the final film structure.

In situ GISAXS is a powerful tool for understanding structure evolution of BCP thin films during solvent or thermal annealing and consequently for optimizing annealing procedures. <sup>40–45</sup> An in situ GISAXS study of the SVA process on as-spun thin films with ISO77-G<sup>A</sup>MR composition was conducted in a flow chamber set up at beamline D1 at Cornell's High Energy Synchrotron Source (CHESS), as described in the Methods section. A Filmetrics reflectometer was used to monitor film thickness, t, changes during SVA, allowing monitoring the swelling ratio (SR =  $t/t_0 - 1$ ) as a function of time, see solid line

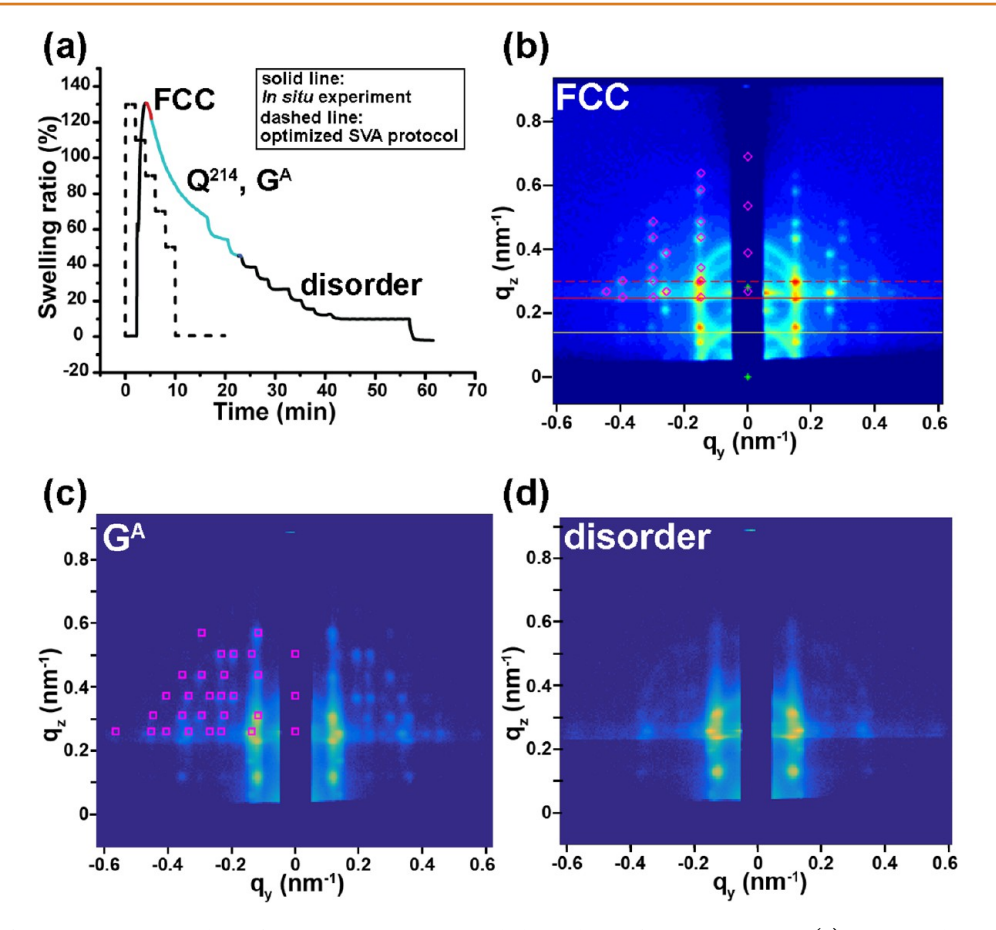


Figure 4. Results of *in situ* GISAXS studies of ISO-77-based BCP-resols hybrid thin films during SVA. (a) Film SR deduced from Filmetrics reflectometer data during SVA (solid line). Red, blue, and black sections correspond to films with FCC,  $G^A$ , and disordered thin-film structure, respectively, as identified by *in situ* GISAXS. A reproducible pathway to thin films with  $G^A$  structure using a simplified SVA set up is approximated in (a) using a dashed line. Representative GISAXS scattering patterns at (b) SR = 130% with incident angle of 0.15°, indexed as FCC (magenta diamonds), (c) SR = 55% with incident angle of 0.14°, indexed as  $G^A$  (magenta squares), and (d) SR = 20% with incident angle of 0.14°, assigned to a film on its way to a disordered state.

in Figure 4a. The as-spun film did not have any ordered structure due to the fast evaporation rate during spin-coating. The film quickly swelled to 130% SR, followed by slow deswelling to around 10% SR via reducing the solvent (THF) partial pressure by controlling the wet (THF in N2 stream) and dry (pure N2 stream) line mixing ratio into the flow chamber as described in the Methods section. Film structure at different swelling stages was monitored and recorded by in situ GISAXS. A representative scattering pattern at highest SR around 130% (red solid line section in Figure 4a) is shown in Figure 4b. The pattern could be indexed by a FCC lattice using indexGIXS software, 46,47 with unit cell parameters of a = b = c = 69 nm,  $\alpha = \beta = \gamma = 90^{\circ}$ , and the (111) plane parallel to the substrate. A FCC structure at the highest film thickness, that is, the highest solvent content, is consistent with micelle formation of a block copolymer in a selective solvent for at least one of the three blocks of the ISO terpolymer. In the region between 125% SR and 45% SR (blue solid line section in Figure 4a), data collected by in situ GISAXS evolved to a distinctly different pattern, as represented in Figure 4c. This scattering pattern was successfully indexed by space group #214 (Q<sup>214</sup>) using GIXSGUI software<sup>37</sup> with unit cell parameters of a = b = c = 65 nm,  $\alpha = \beta = \gamma = 90^{\circ}$ , and the (110) plane parallel to the substrate. When the film was further deswollen to below 45% SR, the structure started to fade as indicated by the GISAXS pattern shown in Figure 4d. Results from this in situ GISAXS study suggest that film structure during SVA strongly depended on the stage of swelling and ordered morphologies did not show any deviation from cubic symmetry (vide supra). Films had to be quenched from the swollen region with  $Q^{214}$  structure (i.e., 45% < SR < 125%) in order to obtain a final film with alternating gyroid structure. The change in symmetry from the swollen cubic (Figure 4c) to the final structure (Figure 3) is most likely due to shrinkage during quenching and pyrolysis of the films. Both processes cause a volume decrease which can most easily be accommodated along the z-direction, as these thin films are constrained in-plane by the substrate, resulting in a uniaxial shrinkage on the way to the final mesoporous film.

Following the insights provided by our *in situ* GISAXS studies, a reproducible SVA procedure leading to G<sup>A</sup> thin-film structure was developed using a simplified SVA chamber as detailed in the Methods section and illustrated in Figure S1, where film thickness was estimated by characteristic film color correlated to the earlier reflectometry results. For comparison, the corresponding approximate annealing pathway to thin films with G<sup>A</sup> structure is plotted as a dashed line in Figure 4a. First, THF vapor flow to the annealing chamber was raised to a high level to ensure a fully swollen film. Then, film SR was decreased stepwise into the region with Q<sup>214</sup> film structure, followed by a fast quench to freeze the alternating gyroid morphology. As suggested by earlier studies, the slower deswelling rate into the Q<sup>214</sup> region may help with the structure formation process.<sup>48</sup>

This SVA procedure was key to obtain thin films with G<sup>A</sup>MR structure as presented in Figures 2a–c and 3.

**Further Characterization of G<sup>A</sup>MR/C Thin Films.** From GISAXS analysis, final ISO69-G<sup>A</sup>MR thin films had smaller unit cell parameters (a = b = 44.8 nm, c = 61.2 nm,  $\alpha = \beta = 90^{\circ}$ ,  $\gamma = 154.2^{\circ}$ , Figure S6) as compared to ISO77-G<sup>A</sup>MR films (a = b = 51.6 nm, c = 71.0 nm,  $\alpha = \beta = 90^{\circ}$ ,  $\gamma = 151.4^{\circ}$ , Figure 3) due to the difference in ISO terpolymer molar mass. In order to further demonstrate the influence of macromolecular design in terms of molar mass on accessible pore sizes of G<sup>A</sup>MR thin films, top surface SEM images of ISO77-G<sup>A</sup>MR and ISO69-G<sup>A</sup>MR thin films were analyzed using ImageJ. Detailed analysis steps are illustrated in Figure S7. Resulting surface pore size distributions are plotted in Figure 5. The observed increase in G<sup>A</sup>MR thin-film

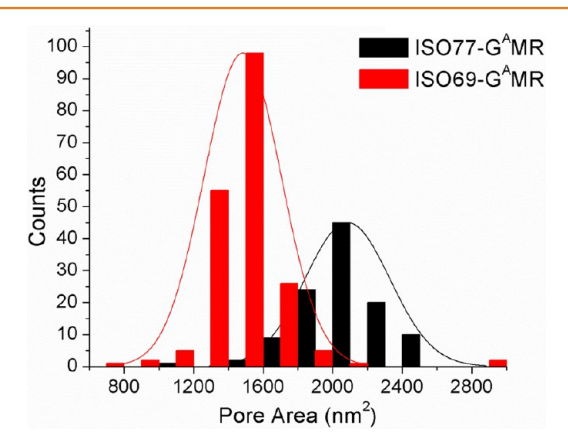


Figure 5. Pore size distribution analysis results of top surface SEM images for ISO69-G<sup>A</sup>MR and ISO77-G<sup>A</sup>MR thin films. Histograms were fitted by a Gaussian distribution with  $\mu = 1461 \text{ nm}^2$  (mean) and  $\sigma = 144 \text{ nm}^2$  (standard deviation) for ISO69-G<sup>A</sup>MR and  $\mu = 2088 \text{ nm}^2$  and  $\sigma = 190 \text{ nm}^2$  for ISO77-G<sup>A</sup>MR.

pore size moving from ISO69 to ISO77 demonstrates tunability through BCP molar mass. Uniaxial shrinkage has little influence on surface pore size distributions as shrinkage is along the film normal direction.

The advantage of GMR thin films in comparison to previously reported polymer templates is that such resin-based materials can endure harsh processing environments such as non-oxidizing strong acids or very high-temperature treatments under inert atmosphere. Previous investigations of bulk films have demonstrated that the terpolymer ISO degrades at around 450 °C, while resols simultaneously convert into highly cross-linked resin material. Above 600 °C, the resin starts to carbonize; that is, the GMR thin films are converted into gyroidal mesoporous carbon, GMC. To that end, we heat treated our GA thin films under nitrogen or argon to 450 °C, 600 °C, and 900 °C, respectively, in a final pyrolysis step. The SEM images of the resulting films depicted in Figure 6a–c suggest that under these conditions the mesoporous gyroidal mesostructure is preserved.

When heated to high temperatures, the resin material undergoes carbonization resulting in electrical conductivity. <sup>24,27,49</sup> As a test, conductivity measurements were performed on mesoporous thin films with G<sup>A</sup> structure heat treated to 450 °C and 900 °C, respectively. For films treated to 900 °C, linear voltage/current sweeps were observed resulting in a sheet resistance value of  $R_s = 455 \text{ k}\Omega \pm 144 \text{ k}\Omega$ , corresponding to a resistivity of 9.1  $\Omega \cdot \text{cm} \pm 2.9 \Omega \cdot \text{cm}$  for an approximated film thickness of 200 nm. In contrast, for films treated to 450 °C, over a voltage range of  $\pm 100 \text{ V}$  the current could not be determined

within the instrument sensitivity of 1 nA, giving a lower bound for the sheet resistance of 453 G $\Omega$ , corresponding to a resistivity of 9.1 M $\Omega$ ·cm for an approximated film thickness of 200 nm. The difference in resistivity by many orders of magnitude between films treated to 450 and 900 °C is consistent with expectations that higher pyrolysis temperatures result in thin-film conductivity. Results also suggest connectivity of the mesoporous carbon thin film over macroscopic dimensions, with no observable major crack formation even under high-temperature conditions.

Since these GMR/C thin films show high-temperature endurance and non-oxidative acid (i.e., hydrofluoric acid) resistance (vide infra), they are compatible with a number of deposition processes used in the semiconductor industry. As a result, they potentially can serve as 3D templates for nanoscale materials formation of various metals or semiconductors. 16,22 A problem commonly encountered during material deposition into templates with such complex 3D structure is that the deposited material cannot completely infiltrate the nanoscale template pores. While the specific deposition method plays an important role, the difference in surface energy/hydrophilicity between template and deposited material is also crucial for successful backfilling. Since the resin material used here undergoes different degrees of carbonization and graphitization when treated at different temperatures, the associated material's chemistry changes are expected to induce changes in surface energy/hydrophilicity. We wanted to elucidate this behavior in more detail. To that end, contact angles were first measured on non-structured resin/carbon thin films in order to eliminate the influence of the porous structure. Flat, dense (nonstructured) thin films were obtained by spin-coating pure resols solutions. The resulting flat thin films (thickness of ~200-400 nm) were then cross-linked, treated at 450 °C, 700 °C, 800 °C, and 1000 °C under inert atmosphere, respectively, and tested for water contact angles. Figure S8 shows SEM images of these dense resin thin films. As depicted in Figure 6d, contact angles substantially decreased as pyrolysis temperature increased, indicating that the resin/carbon materials became more hydrophilic as pyrolysis temperature increased. The same trend was observed for GMR/ C thin films. Contact angle measurements were conducted on ISO69-G<sup>A</sup>MR/C thin films heated to 450 °C, 600 °C, and 900 °C, respectively. Figure 6e again shows decreasing contact angles with increasing pyrolysis temperature, demonstrating similar behavior as for the dense resin materials. The different heat treatment protocols (i.e., different temperatures) provide access to GAMR/C thin films with tunable surface energy/hydrophilicity, which enables fine-tuning of surface characteristics to specific backfilling materials.

GMR Thin-Film Transfer between Different Substrates. In order to increase their applicability as potential 3D templates, we finally demonstrated that these films could be transferred to arbitrary flat substrates. As is well-known in the microelectronics field, substrates are crucial to materials deposition and bottom-up film growth. For instance, electroplating requires a substrate with a conductive seed layer, and vapor—liquid—solid (VLS) growth of Si needs Au as a catalyst, while the epitaxial growth of single crystal structures necessitates a specifically oriented single crystal substrate. Use of GMR thin films as templates in such materials growth/deposition methods would require their fabrication on different substrates. Changing substrates also changes surface energy, however, which in turn changes thin-film—substrate interactions. Indeed, surface energy has been shown to have a substantial influence on SVA of BCPs, 50-52 resulting in time-

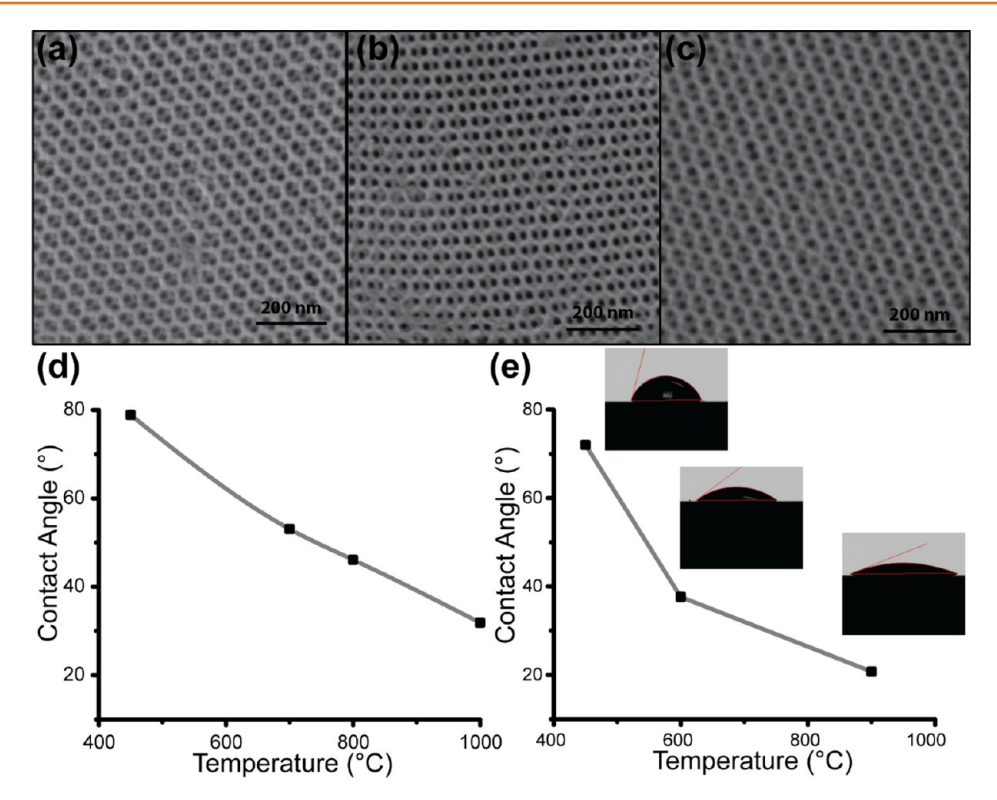


Figure 6. SEM images of ISO69- $G^AMR$  thin films pyrolyzed to (a) 450 °C, (b) 600 °C, and (c) 900 °C, and contact angle measurements for thin-film resin materials heat treated to different temperatures: (d) dense resin/carbon thin films and (e)  $G^AMR/C$  thin films. Gray lines are guides for the eye only.

consuming re-optimization requirements upon substrate switches or even complete failure of desired BCP film formation outcomes. This is particularly true for more complex morphologies like ordered BCP gyroidal structures. Here, we demonstrate that such tedious re-optimization efforts can be avoided altogether by a simple film transfer technique, inspired by a widely used graphene transfer method with PMMA as a protective layer. 32,33

GAMR and GDMR thin-film structures discussed so far were fabricated on Si substrates with native oxide layer typically present on commercially available Si wafers. This oxide layer conveniently served as a sacrificial layer helping thin-film delamination from Si substrates when soaked in a HF-based bath. GMR thin films broke into small pieces, however, when removed from Si substrates in this way. To overcome this problem, a PMMA protective top layer was employed. The resulting transfer process is illustrated in Figure 7a with photos of the different steps shown in Figure 7b-j. A piece of a Si wafer of around 1.5 cm<sup>2</sup> with a G<sup>A</sup>MR thin film on top (Figure 7b) was spin-coated with PMMA solution  $(M_n(PMMA) = 370 \text{ kg/mol},$ PDI = 1.25, Polymer Source; 5 wt % solution in acetone) at 1500 rpm for 30s to form a PMMA protective layer on top of the thin film (Figure 7c). Film edges were subsequently cleaned with a razor blade to help the etching agent, that is, HF, get in contact with the sacrificial oxide layer (Figure 7d). The thin film was then soaked in a buffered oxide etch (BOE) 6:1 (J. T. Baker) solution (Figure 7e). After approximately 3 h, the PMMA/resin composite thin film delaminated from the original silicon wafer and floated to the surface of the etching bath. The film was transferred to a DI water bath (Figure 7f) and carefully scooped out with the target substrate, in this case a gold-coated wafer (Figure 7g). The film on gold was then blow-dried with N<sub>2</sub> helping the film to stabilize on the new substrate (Figure 7h).

Finally, soaking the PMMA/resin composite thin film in acetone overnight removed the PMMA protective layer completing the transfer process (Figure 7i). To further demonstrate the versatility of this process, a GAMR thin film was also transferred onto a flexible substrate (indium tin oxide/ITO-coated PET, 100  $\Omega/\mathrm{sq}$ , Sigma-Aldrich), which is commonly used in microelectronics (Figure 7j). Apart from surface energy effects that would have required time-consuming re-optimization steps for this new substrate, GMR thin-film structures are not directly accessible on such polymer-based substrates due to their incompatibility with high-temperature treatment steps during GMR fabrication.

Figure 8 shows SEM images of thin-film structures after successful transfer onto gold-coated substrates. Top surface and cross-sectional images confirm that both G<sup>A</sup>MR and G<sup>D</sup>MR structures were successfully maintained after transfer onto a gold-coated wafer. In low-magnification SEM images, "wrinkles" were occasionally observed in the transferred G<sup>A</sup>MR thin films (see Figure 8c and d) due to insufficient spreading of the film on the new substrate. SEM images of G<sup>A</sup>MR thin films after transfer onto an ITO-coated PET substrate are shown in Figure S9. We expect this transfer method to work for many different types of flat substrates, which should largely expand the application of these 3D networked thin-film structures in nanomaterials fabrication.

### CONCLUSION

In this report, we demonstrated the synthesis of mesoporous resin or carbon thin films with either alternating or double gyroid 3D structure. For the case of the alternating gyroid structure, we used a combination of *in situ* reflectometry and *in situ* GISAXS to elucidate structural film evolution during SVA, leading to a reproducible pathway to mesoporous resin and carbon thin films

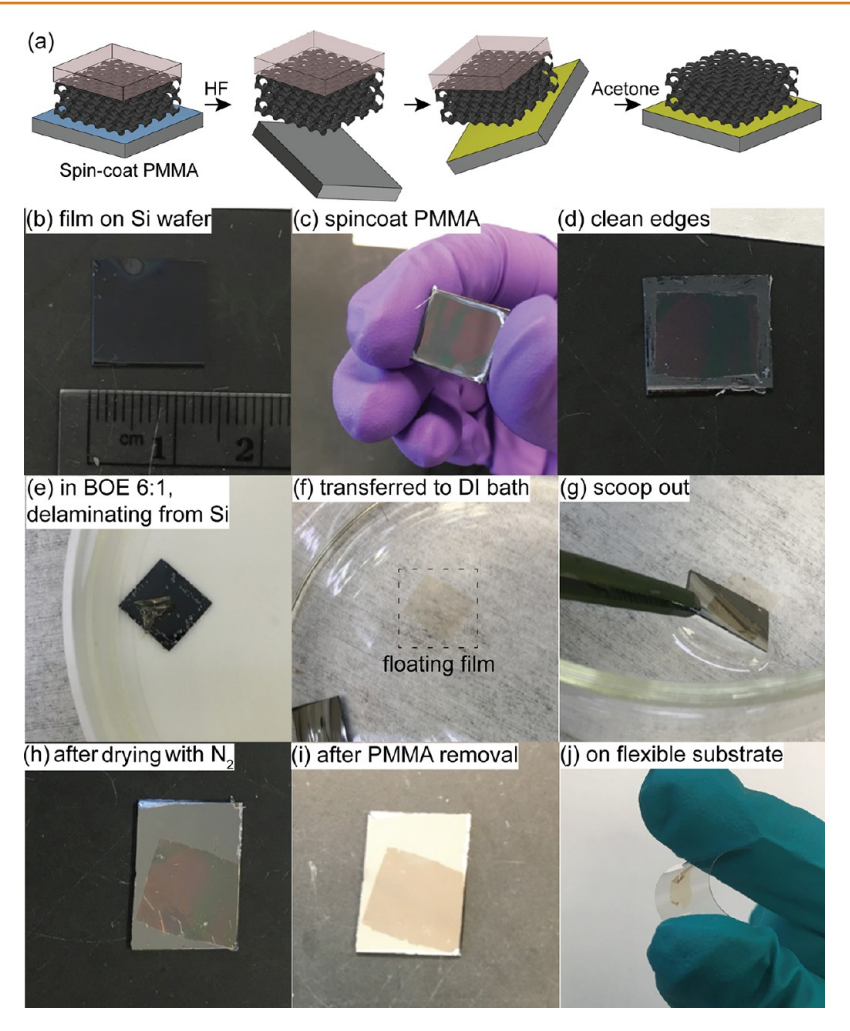


Figure 7. (a) Illustration of GMR thin-film transfer technique and photos taken of different steps during the  $G^AMR$  transfer process onto (b-i) gold-coated wafer and (j) flexible ITO-coated PET.

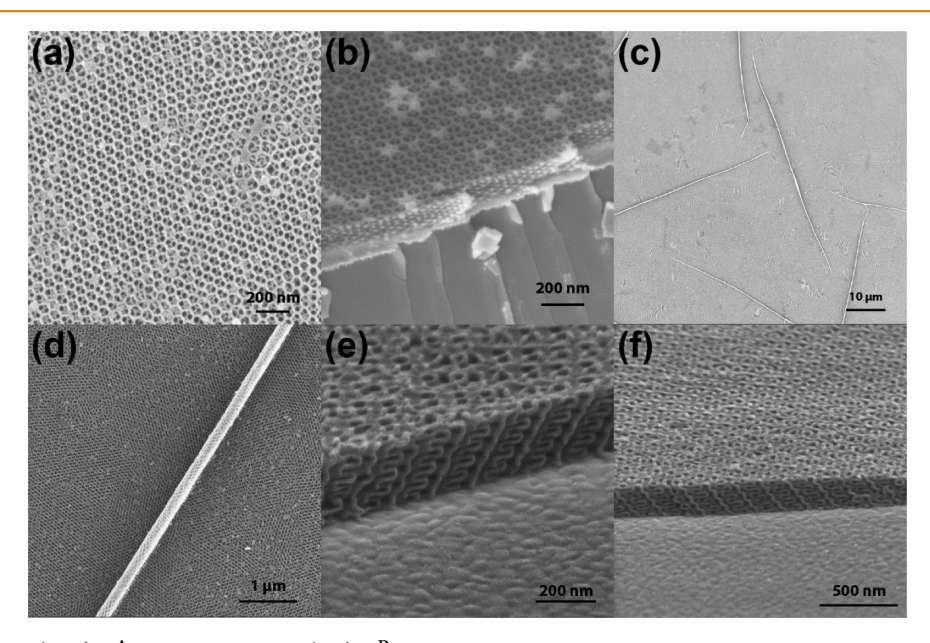


Figure 8. SEM images of (a-d) GAMR thin films and (e, f) GDMR thin films after transfer onto gold-coated substrates.

with this structure. We subsequently highlighted the versatility of the resulting 3D structure for nanomaterials formation: Thinfilm pore size could be tailored by ISO molar mass, and pore surface energy/hydrophilicity could be tuned by heating to different temperatures between 400 and 1000  $^{\circ}$ C. This is expected to be beneficial for materials deposition into the small

nanoscale pores by allowing to match template surface energy to that of the backfilling material. High-temperature durability under inert gas environments renders thin films compatible with typical deposition methods used in the microelectronics industry such as CVD. It simultaneously provides functional templates with electrical conductivity as required, for example, in on-chip battery devices. The demonstrated ability to transfer these thin films to other desired substrates eliminates time-consuming reoptimization steps of thin-film formation, enables the use of substrates that otherwise are not compatible with hightemperature formation steps (e.g., flexible polymer substrates), and tremendously expands the use of these potential 3D templates for various established backfilling and growth techniques. With these results, the GMR/C thin films reported in this work present an advanced materials platform, which we hope will be useful to a range of fundamental and applied nanomaterials research efforts at the characteristic sub-100 nm length scale.

### **METHODS**

**Synthesis.** Three ISO terpolymers with number average molar mass,  $M_{\rm n}$ , of 77, 69, and 28 kg/mol (i.e., ISO77, ISO69, and ISO28) and varying compositions were synthesized via sequential anionic polymerization, as described previously.<sup>54</sup> Polymer characterization details are listed in Table 1. Oligomeric resorcinol-formaldehyde resols and phenol-formaldehyde resols were synthesized via well-known polymerization of resorcinol/phenol and formaldehyde under basic conditions as described in ref 24. Resorcinol-formaldehyde resols and phenolformaldehyde resols were both characterized by GPC in THF with UV detector at 254 nm wavelength. GPC traces of resorcinol-formaldehyde resols and phenol-formaldehyde resols as well as of resorcinol and phenol molecules are shown in Figure S10. By comparing Figure S10a,b as well as Figure S10c,d, we see that the peaks at elution volumes of 9.7 mL are from unreacted resorcinol or phenol molecules, respectively. We therefore only integrated the parts that eluted faster than these peaks for resorcinol-formaldehyde and phenol-formaldehyde resols' molar mass assessements, respectively. From these analyses, resorcinol-formaldehyde and phenol-formaldehyde resols were, respectively characterized as follows:  $M_n = 580 \text{ g/mol}, M_w = 630, \text{ and PDI} = 1.08; M_n = 360$ g/mol,  $M_{\rm w}$  = 370 g/mol, and PDI = 1.02 (using PS standards in both cases).

Thin-Film Preparation. Two types of gyroidal mesoporous resin thin films with either alternating gyroid  $(G^AMR)$  or double gyroid  $(G^DMR)$  structure were achieved.  $G^AMR$  formation started with an ISO plus resorcinol-resols hybrid solution, while GDMR formation started with an ISO plus phenol-resols hybrid solution. The amount of resols added to the solutions was calculated to match the PEO + resols weight percentage as listed in Table 1. The final ISO + resols solutions had a total concentration of 5 wt % in THF for resorcinol-resols-based solutions and 10 wt % in THF for phenol-resols-based solutions, respectively. ISO terpolymers were dissolved in THF and stirred for 30 min, followed by the addition of resols stock solution. After stirring for another 1 h for ISO + resorcinol-resols solutions and 24 h for ISO + phenol-resols solutions, thin films were spin-coated in a drybox with relative humidity maintained below 30%. Two types of thin films with targeted alternating gyroidal mesoporous resin structure, that is, ISO69-GAMR and ISO77-GAMR, were spin-coated on silicon substrates at a speed of 3000 rpm for 1 min. Films with targeted double gyroidal mesoporous resin structure, ISO28-GDMR, were spin-coated on silicon substrates at a speed of 1000 rpm for 1 min. As-spun films were subjected to different solvent annealing procedures to achieve the desired mesostructures. Films with targeted GA structure were annealed in THF vapor at room temperature (24 °C) in a flow chamber illustrated in Figure S1. Dry nitrogen gas (N2) was passed through two flow meters. One N<sub>2</sub> stream then went directly into the annealing chamber, referred as the dry line. Another  $N_2$  stream went into a THF solvent reservoir after passing the flow meter and before entering the annealing chamber,

referred to as the wet line. The annealing chamber was adapted from a cylindrical bottle with a bottom diameter of 4.5 cm and a height of 9.5 cm. The solvent reservoir was adapted from a conical flask with a bottom diameter of 7.5 cm and a height of 13 cm. The volume of THF in the solvent reservoir was kept around 175 mL. By adjusting flow rates of dry and wet lines, different SRs of the films were achieved. At the beginning of the solvent annealing process, the flow rates of dry and wet lines were set as 1.5 SCFH (wet) and 0.2 SCFH (dry) to achieve a relatively high SR. Flow rates were then adjusted stepwise every 2 min to 1.5 SCFH (wet) and 0.3 SCFH (dry), 1.5 SCFH (wet) and 0.4 SCFH (dry), 1.25 SCFH (wet) and 0.4 SCFH (dry), and 1 SCFH (wet) and 0.4 SCFH (dry) to slowly decrease the SR of the thin film. After staying at 1 SCFH (wet) and 0.4 SCFH (dry) for 2 min, the films were quenched by closing the wet line flow and increasing the dry line flow to its maximum.

For films with targeted G<sup>D</sup> structure, the as-spun thin films were first placed onto a vial turned upside down serving as a stage. The film, vial, and a Petri dish filled with 10 mL of chloroform were then put under a glass dome. The set up was heated on a hot plate at 50 °C for 1 h, then removed from the hot plate and left under ambient conditions until the remaining chloroform evaporated, usually approximately 40 h.

After solvent annealing, thin films were cured in an oven at 115 °C for 24 h to cross-link the resols. Surface capping layers were observed for thin films with double gyroid morphology, hence an extra etching step was required. To that end, cured  $G^D$  films were treated with tetrafluoromethane (CF<sub>4</sub>) plasma at forward power of 150 W for 4 min to remove the capping layers in an Oxford PlasmaLab 80+ RIE System. After cross-linking (and surface etching for  $G^D$  samples), thin films were heated at a rate of 1 °C min<sup>-1</sup> to 450 °C and pyrolyzed under inert atmosphere (nitrogen or argon) at 450 °C for 3 h, generating  $G^A$ MR or  $G^D$ MR thin films. Thin films pyrolyzed at higher temperatures were brought to the final temperature at a rate of 1 °C/min after being stabilized at 450 °C for 3 h, then remained at the final temperature for another 3 h. Such heat treatments at final temperatures of 600 °C or higher generated gyroidal mesoporous carbon (GMC) thin films.

**Preparation of Gold-Coated Wafers.** Gold-coated Si wafers were either purchased from Sigma-Aldrich (99.999% (Au), layer thickness 1000 Å, with titanium as an adhesion layer to bind gold to the silicon wafer) or prepared *via* thermally evaporating gold onto Si wafers using CHA SE-600 thermal evaporator. To that end, a 10 nm Cr adhesive layer was first evaporated at a speed of 1 Å/s. A gold layer was subsequently evaporated at a speed of 1 Å/s. The final thickness of the gold layer was around 10 nm.

Materials Characterization. Triblock terpolymer molar mass, composition, and polydispersity were determined by a combination of gel permeation chromatography (GPC) and <sup>1</sup>H nuclear magnetic resonance (<sup>1</sup>H NMR) spectroscopy. SEM images of thin films were acquired on a Tescan LM Mira3 FE-SEM with an in-lens detector. GISAXS patterns of thin-film structures as shown in Figure 3 were acquired at Sector 8-ID-E<sup>55</sup> at the Advanced Photon Source at Argonne National Laboratory with sample-to-detector distance of 2.2 m and incident photon energy of 10.86 keV. Patterns were recorded with a Dectris Pilatus 1 M detector, and the X-ray beam was 20 µm in height and 100  $\mu$ m in width. GISAXS patterns as shown in Figure S6 were acquired at beamline G1 at Cornell's High Energy Synchrotron Source (CHESS), with sample-to-detector distance of 2.2 m and incident photon energy of 9.83 keV. Patterns were recorded on a Dectris Pilatus3–200k pixel array detector with an incident beam of 250  $\mu$ m  $\times$ 250  $\mu m$  defined using a standard three-slit setup.

Combined in Situ GISAXS/Reflectometry Measurements during Solvent Vapor Annealing. In situ GISAXS patterns shown in Figure 4 were acquired at beamline D1 at CHESS, with sample-to-detector distance of 1.8 m and incident photon energy of 10.6 keV. Patterns were recorded on a Dectris Pilatus3–200k pixel array detector. A custom-built vapor annealing chamber used during in situ GISAXS experiments was set up at CHESS beamline D1. An illustration depicting the apparatus is shown in Figure S2 (for a photograph of the annealing chamber see Figure 6 of ref 40). The solvent vapor concentration inside the chamber was controlled by  $N_2$  passing through two flow meters. One  $N_2$  stream after passing a first flow meter went directly into the annealing chamber and will be referred to as the "dry line". Another  $N_2$  stream after

passing a second flow meter first was bubbled through a THF solvent reservoir before entering the annealing chamber and will be referred to as the "wet line". Wet and dry lines mixed before entering the annealing chamber. Two flow meters controlling wet and dry lines were tuned constantly during annealing to maintain the desired solvent-swollen film thickness, which was monitored *in situ* by optical reflectometry measurements (FilMetrics F30 reflectometer). Thickness measurements were taken at a spot which did not get exposed to X-rays during *in situ* GISAXS measurements. Both GISAXS patterns and reflectometry measurements were collected automatically every 5 s during the SVA process.

**Conductivity Measurements.** Conductivity measurements were performed by directly contacting the surfaces of films treated at 450 and 900 °C using an in-line four-point probe setup (Everbeing International Corp.) with a Keithley 2400 sourcemeter. Voltage (V)—current (I) sweeps were performed for 4 spatial points on each film over the range of  $\pm$ 7 V for the 900 °C films and  $\pm$ 100 V for the 450 °C films. Sweeps were linear in all cases. Linear slopes were employed to calculate sheet resistance ( $R_s$ ) using the well-known equation in the limit of a very thin film relative to the probe spacing of  $R_s = \pi/\ln(2)V/I$ . Resistivity was also calculated using  $R = R_s \times t$ , with an approximated film thickness, t. The films tested were fabricated on thermally grown SiO<sub>2</sub> (100 nm) to eliminate conductivity contributions from substrates.

### **ASSOCIATED CONTENT**

# **S** Supporting Information

The Supporting Information is available free of charge on the ACS Publications website at DOI: 10.1021/acsnano.7b06436.

Further setup illustrations, electron microscopy and GISAXS analysis are provided. Resols GPC traces, detailed descriptions of thin-film shrinkage and pore size distribution analysis are also provided (PDF)

## **AUTHOR INFORMATION**

## **Corresponding Author**

\*Email: ubw1@cornell.edu.

### ORCID ®

Qi Zhang: 0000-0001-5765-4505

Detlef-M. Smilgies: 0000-0001-9351-581X Kwan Wee Tan: 0000-0002-8289-6503 Jörg G. Werner: 0000-0001-7845-086X Paul F. Nealey: 0000-0003-3889-142X Ulrich B. Wiesner: 0000-0001-6934-3755

# Notes

The authors declare no competing financial interest.

# **ACKNOWLEDGMENTS**

This work was funded by the National Science Foundation (DMR-1707836). P.A.B. was supported by the NSF Graduate Research Fellowship Program (DGE-1650441). This work made use of the Cornell Center for Materials Research Shared Facilities, which are supported through the NSF MRSEC program (DMR-1719875), Cornell NanoScale Facility (CNF), a member of the National Nanotechnology Coordinated Infrastructure (NNCI), which is supported by the National Science Foundation (Grant ECCS-1542081), the Cornell High Energy Synchrotron Source (CHESS), which is supported by the National Science Foundation under award DMR-1332208, and the Advanced Photon Source (APS), a U.S. Department of Energy (DOE) Office of Science User Facility operated for the DOE Office of Science by Argonne National Laboratory under contract no. DE-AC02-06CH11357. Q.Z acknowledges Y. Li (Wiesner group, Cornell University), K. Barteau (Wiesner

group, Cornell University), M. Dolejsi (Nealey group, University of Chicago), and T. Segal-Peretz (Nealey group, University of Chicago) for helpful discussions. H.S.S. and S.X. acknowledge Z. Jiang (APS) for his help with beamline setup. H.S.S., S.X. and P.F.N gratefully acknowledge support by U.S. Department of Energy, Basic Energy Sciences, Argonne National Laboratory, Materials Sciences, and Engineering Division for aspects of the work related to GISAXS and solvent vapor annealing. K.W.T. acknowledges a startup grant from Nanyang Technological University.

## **REFERENCES**

- (1) Zhang, H.; Yu, X.; Braun, P. V. Three-Dimensional Bicontinuous Ultrafast-Charge and-Discharge Bulk Battery Electrodes. *Nat. Nanotechnol.* **2011**, *6*, 277–281.
- (2) Kim, O. H.; Cho, Y. H.; Kang, S. H.; Park, H. Y.; Kim, M.; Lim, J. W.; Chung, D. Y.; Lee, M. J.; Choe, H.; Sung, Y. E. Ordered Macroporous Platinum Electrode and Enhanced Mass Transfer in Fuel Cells Using Inverse Opal Structure. *Nat. Commun.* **2013**, *4*, 2473.
- (3) Kim, J. E.; Oh, J. H.; Kotal, M.; Koratkar, N.; Oh, I. K. Self-Assembly and Morphological Control of Three-Dimensional Macroporous Architectures Built of Two-Dimensional Materials. *Nano Today* **2017**, *14*, 100–123.
- (4) Braun, P. V. Materials Chemistry in 3D Templates for Functional Photonics. *Chem. Mater.* **2014**, *26*, 277–286.
- (5) Hur, K.; Francescato, Y.; Giannini, V.; Maier, S. A.; Hennig, R. G.; Wiesner, U. Three-Dimensionally Isotropic Negative Refractive Index Materials from Block Copolymer Self-Assembled Chiral Gyroid Networks. *Angew. Chem., Int. Ed.* **2011**, *50*, 11985–11989.
- (6) Bauer, J.; Schroer, A.; Schwaiger, R.; Kraft, O. Approaching Theoretical Strength in Glassy Carbon Nanolattices. *Nat. Mater.* **2016**, 15, 438–443.
- (7) Lee, J. H.; Singer, J. P.; Thomas, E. L. Micro-/Nanostructured Mechanical Metamaterials. *Adv. Mater.* **2012**, *24*, 4782–4810.
- (8) Valev, V. K.; Baumberg, J. J.; Sibilia, C.; Verbiest, T. Chirality and Chiroptical Effects in Plasmonic Nanostructures: Fundamentals, Recent progress, and Outlook. *Adv. Mater.* **2013**, 25, 2517–2534.
- (9) Salvatore, S.; Demetriadou, A.; Vignolini, S.; Oh, S. S.; Wuestner, S.; Yufa, N. A.; Stefik, M.; Wiesner, U.; Baumberg, J. J.; Hess, O.; Steiner, U. Tunable 3D Extended Self-Assembled Gold Metamaterials with Enhanced Light Transmission. *Adv. Mater.* **2013**, *25*, 2713–2716.
- (10) Dolan, J. A.; Wilts, B. D.; Vignolini, S.; Baumberg, J. J.; Steiner, U.; Wilkinson, T. D. Optical Properties of Gyroid Structured Materials: from Photonic Crystals to Metamaterials. *Adv. Opt. Mater.* **2015**, *3*, 12–32.
- (11) Shimmin, R. G.; Vajtai, R.; Siegel, R. W.; Braun, P. V. Room-Temperature Assembly of Germanium Photonic Crystals through Colloidal Crystal Templating. *Chem. Mater.* **2007**, *19*, 2102–2107.
- (12) von Freymann, G.; Kitaev, V.; Lotsch, B. V.; Ozin, G. A. Bottom-Up Assembly of Photonic Crystals. *Chem. Soc. Rev.* **2013**, 42, 2528–2554.
- (13) Tan, K. W.; Saba, S. A.; Arora, H.; Thompson, M. O.; Wiesner, U. Colloidal Self-Assembly-Directed Laser-Induced Non-Close-Packed Crystalline Silicon Nanostructures. *ACS Nano* **2011**, *5*, 7960–7966.
- (14) Selimis, A.; Mironov, V.; Farsari, M. Direct laser writing: Principles and Materials for Scaffold 3D Printing. *Microelectron. Eng.* **2015**, *132*, 83–89.
- (15) Brüser, B.; Staude, I.; von Freymann, G.; Wegener, M.; Pietsch, U. Visible Light Laue Diffraction from Woodpile Photonic Crystals. *Appl. Opt.* **2012**, *51*, 6732–6737.
- (16) Arora, H.; Du, P.; Tan, K. W.; Hyun, J. K.; Grazul, J.; Xin, H. L.; Muller, D. A.; Thompson, M. O.; Wiesner, U. Block Copolymer Self-Assembly—Directed Single-Crystal Homo-and Heteroepitaxial Nanostructures. *Science* **2010**, 330, 214–219.
- (17) Park, S.; Kim, Y.; Ahn, H.; Kim, J. H.; Yoo, P. J.; Ryu, D. Y. Giant Gyroid and Templates from High-Molecular-Weight Block Copolymer Self-assembly. *Sci. Rep.* **2016**, *6*, 36326.

(18) Crossland, E. J.; Kamperman, M.; Nedelcu, M.; Ducati, C.; Wiesner, U.; Smilgies, D. M.; Toombes, G. E.; Hillmyer, M. A.; Ludwigs, S.; Steiner, U.; Snaith, H. J. A Bicontinuous Double Gyroid Hybrid Solar Cell. *Nano Lett.* **2009**, *9*, 2807–2812.

- (19) Scherer, M. R.; Li, L.; Cunha, P.; Scherman, O. A.; Steiner, U. Enhanced Electrochromism in Gyroid-Structured Vanadium Pentoxide. *Adv. Mater.* **2012**, 24, 1217–1221.
- (20) Scherer, M. R.; Steiner, U. Efficient Electrochromic Devices Made from 3D Nanotubular Gyroid Networks. *Nano Lett.* **2013**, *13*, 3005–3010.
- (21) Salvatore, S.; Vignolini, S.; Philpott, J.; Stefik, M.; Wiesner, U.; Baumberg, J. J.; Steiner, U. A High Transmission Wave-Guide Wire Network Made by Self-assembly. *Nanoscale* **2015**, *7*, 1032–1036.
- (22) Cowman, C. D.; Padgett, E.; Tan, K. W.; Hovden, R.; Gu, Y.; Andrejevic, N.; Muller, D.; Coates, G. W.; Wiesner, U. Multicomponent Nanomaterials with Complex Networked Architectures from Orthogonal Degradation and Binary Metal Backfilling in ABC Triblock Terpolymers. J. Am. Chem. Soc. 2015, 137, 6026–6033.
- (23) Hsueh, H. Y.; Yao, C. T.; Ho, R. M. Well-Ordered Nanohybrids and Nanoporous Materials from Gyroid Block Copolymer Templates. *Chem. Soc. Rev.* **2015**, *44*, 1974–2018.
- (24) Werner, J. G.; Hoheisel, T. N.; Wiesner, U. Synthesis and Characterization of Gyroidal Mesoporous Carbons and Carbon Monoliths with Tunable Ultralarge Pore Size. *ACS Nano* **2014**, *8*, 731–743.
- (25) Werner, J. G.; Johnson, S. S.; Vijay, V.; Wiesner, U. Carbon-Sulfur Composites from Cylindrical and Gyroidal Mesoporous Carbons with Tunable Properties in Lithium-Sulfur Batteries. *Chem. Mater.* **2015**, *27*, 3349–3357.
- (26) Werner, J. G.; Scherer, M. R. J.; Steiner, U.; Wiesner, U. Gyroidal Mesoporous Multifunctional Nanocomposites *via* Atomic Layer Deposition. *Nanoscale* **2014**, *6*, 8736–8742.
- (27) Tan, K. W.; Jung, B.; Werner, J. G.; Rhoades, E. R.; Thompson, M. O.; Wiesner, U. Transient Laser Heating Induced Hierarchical Porous Structures from Block Copolymer–Directed Self-Assembly. *Science* **2015**, 349, 54–58.
- (28) Deng, G.; Zhang, Y.; Ye, C.; Qiang, Z.; Stein, G. E.; Cavicchi, K. A.; Vogt, B. D. Bicontinuous Mesoporous Carbon Thin Films *via* an Order–Order Transition. *Chem. Commun.* **2014**, *50*, 12684–12687.
- (29) Qiang, Z.; Xue, J.; Cavicchi, K. A.; Vogt, B. D. Morphology Control in Mesoporous Carbon Films Using Solvent Vapor Annealing. *Langmuir* **2013**, *29*, 3428–3438.
- (30) Zhou, Z.; Liu, G. Controlling the Pore Size of Mesoporous Carbon Thin Films through Thermal and Solvent Annealing. *Small* **2017**, *13*, 1603107.
- (31) Albert, J. N.; Epps, T. H. Self-Assembly of Block Copolymer Thin Films. *Mater. Today* **2010**, *13*, 24–33.
- (32) Gao, T.; Li, Z.; Huang, P. S.; Shenoy, G. J.; Parobek, D.; Tan, S.; Lee, J. K.; Liu, H.; Leu, P. W. Hierarchical Graphene/Metal Grid Structures for Stable, Flexible Transparent Conductors. *ACS Nano* **2015**, *9*, 5440–5446.
- (33) Li, X.; Zhu, Y.; Cai, W.; Borysiak, M.; Han, B.; Chen, D.; Piner, R. D.; Colombo, L.; Ruoff, R. S. Transfer of Large-Area Graphene Films for High-Performance Transparent Conductive Electrodes. *Nano Lett.* **2009**, *9*, 4359–4363.
- (34) Gurarslan, A.; Yu, Y.; Su, L.; Yu, Y.; Suarez, F.; Yao, S.; Zhu, Y.; Ozturk, M.; Zhang, Y.; Cao, L. Surface-Energy-Assisted Perfect Transfer of Centimeter-Scale Monolayer and Few-Layer MoS2 Films onto Arbitrary Substrates. ACS Nano 2014, 8, 11522—11528.
- (35) Feng, D.; Lv, Y.; Wu, Z.; Dou, Y.; Han, L.; Sun, Z.; Xia, Y.; Zheng, G.; Zhao, D. Free-Standing Mesoporous Carbon Thin Films with Highly Ordered Pore Architectures for Nanodevices. *J. Am. Chem. Soc.* **2011**, *133*, 15148–15156.
- (36) Chatterjee, J.; Jain, S.; Bates, F. S. Comprehensive Phase Behavior of Poly(Isoprene-b-Styrene-b-Ethylene Oxide) Triblock Copolymers. *Macromolecules* **2007**, *40*, 2882–2896.
- (37) Jiang, Z. GIXSGUI: a MATLAB Toolbox for Grazing-Incidence X-Ray Scattering Data Visualization and Reduction, and Indexing of

Buried Three-Dimensional Periodic Nanostructured Films. *J. Appl. Crystallogr.* **2015**, 48, 917–926.

- (38) Epps, T. H.; Cochran, E. W.; Bailey, T. S.; Waletzko, R. S.; Hardy, C. M.; Bates, F. S. Ordered Network Phases in Linear Poly (Isoprene-b-Styrene-b-Ethylene Oxide) Triblock Copolymers. *Macromolecules* **2004**, 37, 8325–8341.
- (39) Tanaka, S.; Katayama, Y.; Tate, M. P.; Hillhouse, H. W.; Miyake, Y. Fabrication of Continuous Mesoporous Carbon Films with Face-Centered Orthorhombic Symmetry through a Soft Templating Pathway. *J. Mater. Chem.* **2007**, *17*, 3639–3645.
- (40) Posselt, D.; Zhang, J.; Smilgies, D. M.; Berezkin, A. V.; Potemkin, I. I.; Papadakis, C. M. Restructuring in Block Copolymer Thin Films: *In Situ* GISAXS Investigations during Solvent Vapor Annealing. *Prog. Polym. Sci.* **2017**, *66*, 80–115.
- (41) Schuster, J.; Köhn, R.; Döblinger, M.; Keilbach, A.; Amenitsch, H.; Bein, T. *In Situ* SAXS Study on a New Mechanism for Mesostructure Formation of Ordered Mesoporous Carbons: Thermally Induced Self-Assembly. *J. Am. Chem. Soc.* **2012**, *134*, 11136–11145.
- (42) Chavis, M. A.; Smilgies, D. M.; Wiesner, U. B.; Ober, C. K. Widely Tunable Morphologies in Block Copolymer Thin Films through Solvent Vapor Annealing Using Mixtures of Selective Solvents. *Adv. Funct. Mater.* **2015**, 25, 3057–3065.
- (43) Bai, W.; Yager, K. G.; Ross, C. A. *In Situ* Characterization of the Self-Assembly of a Polystyrene–Polydimethylsiloxane Block Copolymer During Solvent Vapor Annealing. *Macromolecules* **2015**, 48, 8574–8584.
- (44) Shin, C.; Ryu, D. Y.; Huh, J.; Kim, J. H.; Kim, K. W. Order-to-Order Transitions of Block Copolymer in Film Geometry. *Macromolecules* **2009**, *42*, 2157–2160.
- (45) Shelton, C. K.; Epps, T. H. Block Copolymer Thin Films: Characterizing Nanostructure Evolution with *in Situ* X-Ray and Neutron Scattering. *Polymer* **2016**, *105*, 545–561.
- (46) Smilgies, D. M.; Blasini, D. R. Indexation Scheme for Oriented Molecular Thin Films Studied with Grazing-Incidence Reciprocal-Space Mapping. *J. Appl. Crystallogr.* **2007**, *40*, 716–718.
- (47) Busch, P.; Rauscher, M.; Smilgies, D. M.; Posselt, D.; Papadakis, C. M. Grazing-Incidence Small-Angle X-Ray Scattering (GISAXS) from Thin, Nanostructured Block Copolymer Films—The Scattering Cross-Section in the Distorted-Wave Born Approximation. *J. Appl. Crystallogr.* **2006**, *39*, 433.
- (48) Albert, J. N.; Young, W. S.; Lewis, R. L., III; Bogart, T. D.; Smith, J. R.; Epps, T. H., III Systematic Study on the Effect of Solvent Removal Rate on the Morphology of Solvent Vapor Annealed ABA Triblock Copolymer Thin Films. *ACS Nano* **2012**, *6*, 459–466.
- (49) Li, X.; Larson, A. B.; Jiang, L.; Song, L.; Prichard, T.; Chawla, N.; Vogt, B. D. Evolution of Mechanical, Optical and Electrical Properties of Self-Assembled Mesostructured Phenolic Resins during Carbonization. *Microporous Mesoporous Mater.* **2011**, *138*, 86–93.
- (50) Epps, T. H.; DeLongchamp, D. M.; Fasolka, M. J.; Fischer, D. A.; Jablonski, E. L. Substrate Surface Energy Dependent Morphology and Dewetting in an ABC Triblock Copolymer Film. *Langmuir* **2007**, 23, 3355–3362.
- (51) Sinturel, C.; Vayer, M.; Morris, M.; Hillmyer, M. A. Solvent Vapor Annealing of Block Polymer Thin Films. *Macromolecules* **2013**, *46*, 5399–5415.
- (52) Wan, L.; Ji, S.; Liu, C. C.; Craig, G. S.; Nealey, P. F. Directed Self-Assembly of Solvent-Vapor-Induced Non-Bulk Block Copolymer Morphologies on Nanopatterned Substrates. *Soft Matter* **2016**, *12*, 2914–2922.
- (53) Mannsfeld, S. C.; Tee, B. C.; Stoltenberg, R. M.; Chen, C. V. H.; Barman, S.; Muir, B. V.; Sokolov, A. N.; Reese, C.; Bao, Z. Highly Sensitive Flexible Pressure Sensors with Microstructured Rubber Dielectric Layers. *Nat. Mater.* **2010**, *9*, 859–864.
- (54) Bailey, T. S.; Hardy, C. M.; Epps, T. H.; Bates, F. S. A Noncubic Triply Periodic Network Morphology in Poly (Isoprene-b-Styrene-b-Ethylene Oxide) Triblock Copolymers. *Macromolecules* **2002**, *35*, 7007–7017.
- (55) Jiang, Z.; Li, X.; Strzalka, J.; Sprung, M.; Sun, T.; Sandy, A. R.; Narayanan, S.; Lee, D. R.; Wang, J. The Dedicated High-Resolution

Grazing-Incidence X-Ray Scattering Beamline 8-ID-E at the Advanced Photon Source. *J. Synchrotron Radiat.* **2012**, *19*, 627–636.